AGU PUBLICATIONS

JGR

Journal of Geophysical Research: Space Physics

RESEARCH ARTICLE
10.1002/2016JA023811

Key Points:
- Efficiently excite 3-D Alfvén resonances in time-dependent numerical simulations
- Describe the family of possible solutions of resonant Alfvén waves
- Provide analytical estimates for resonance widths and amplitudes in 3-D

Correspondence to:
T. Elsden,
te55@st-andrews.ac.uk

Citation:
Elsden, T., and A. N. Wright (2017), The theoretical foundation of 3-D Alfvén resonances: Time-dependent solutions, *J. Geophys. Res. Space Physics*, *122*, 3247–3261, doi:10.1002/2016JA023811.

Received 19 DEC 2016
Accepted 28 FEB 2017
Accepted article online 9 MAR 2017
Published online 20 MAR 2017

The theoretical foundation of 3-D Alfvén resonances: Time-dependent solutions

T. Elsden[1] **and A. N. Wright**[1]

[1]Department of Mathematics and Statistics, University of St Andrews, St Andrews, UK

Abstract We present results from a 3-D numerical simulation which investigates the coupling of fast and Alfvén magnetohydrodynamic (MHD) waves in a nonuniform dipole equilibrium. This represents the time-dependent extension of the normal mode ($\propto \exp(-i\omega t)$) analysis of Wright and Elsden (2016) and provides a theoretical basis for understanding 3-D Alfvén resonances. Wright and Elsden (2016) show that these are fundamentally different to resonances in 1-D and 2-D. We demonstrate the temporal behavior of the Alfvén resonance, which is formed within the "Resonant Zone"; a channel of the domain where a family of solutions exists such that the natural Alfvén frequency matches the fast-mode frequency. At early times, phase mixing leads to the production of prominent ridges in the energy density, whose shape is determined by the Alfvén speed profile and the chosen background magnetic field geometry. These off resonant ridges decay in time, leaving only a main 3-D resonant sheet in the steady state. We show that the width of the 3-D resonance in time and in space can be accurately estimated by adapting previous analytical estimates from 1-D theory. We further provide an analytical estimate for the resonance amplitude in 3-D, based upon extending 2-D theory.

1. Introduction

This work is concerned with the coupling of fast and Alfvén magnetohydrodynamic (MHD) waves. Resonant coupling will occur at the location where the Alfvén frequency matches the fast-mode frequency in a process known as resonant absorption or field line resonance (FLR). This process has applications in both solar and magnetospheric settings but is treated here in a theoretical sense.

There have been many theoretical and computational studies on Alfvén resonances with varying degrees of complexity. They may broadly be classified according to the number of independent spatial coordinates the mathematical formulation of the problem depends upon. For example, *Southwood* [1974] assumed Fourier modes in both the field-aligned and azimuthal directions and time, reducing the problem to an ordinary differential equation in the radial coordinate. This approach (along with that of *Chen and Hasegawa* [1974]) provides much insight and reveals the Alfvén resonance as a singularity in a 1-D model. These waves represent Alfvén waves standing on geomagnetic field lines, a concept first theorized by *Dungey* [1954, 1967].

Subsequently, the theory has been refined in many aspects: Computational 1-D models including time dependence were studied by *Allan et al.* [1985, 1986a, 1986b] and *Mann et al.* [1995] and were extended to 2-D by *Lee and Lysak* [1989, 1990]. The latter clearly showed the persistence of FLRs in 2-D axisymmetric equilibria. Subsequent normal mode (i.e., solutions $\propto \exp(-i\omega t)$) studies put this on a firm theoretical basis [*Southwood and Kivelson*, 1986; *Thompson and Wright*, 1993; *Wright and Thompson*, 1994]. Further details of these and other studies can be found in the review by *Wright and Mann* [2006].

More recently, time-dependent 3-D simulations have provided evidence for the persistence of Alfvén resonances in 3-D [*Claudepierre et al.*, 2009, 2010; *Degeling et al.*, 2010; *Terradas et al.*, 2016]. A theoretical framework for understanding 3-D Alfvén resonances has been described recently by *Wright and Elsden* [2016] and shows that Alfvén resonances in 3-D are fundamentally different to those in 1-D and 2-D. In particular, identifying the location of resonant coupling and the polarization is not straightforward as there is no longer a unique solution, in fact there are an infinite number.

1.1. 3-D Field Line Resonances

To appreciate why 3-D FLRs are different to those in 1-D and 2-D, consider the cases depicted in Figure 1 which shows the intersection of both the magnetopause boundary and the resonant field lines with the equatorial

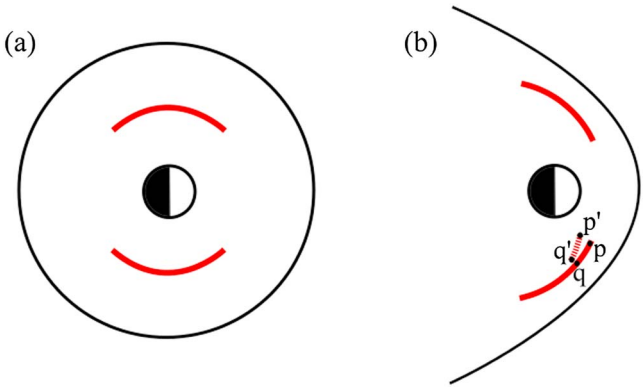

Figure 1. Intersection with the equatorial plane of a model magnetosphere in (a) an axisymmetric case and (b) a flared nonaxisymmetric case, with the Sun to the right. The outer black lines represent a notional magnetopause, the red lines (solid and dashed) possible resonant locations. Points p, q, p′ and q′ represent resonant field lines which are further explained in the main text.

plane. Figure 1a shows an idealized equilibrium (e.g., based upon a dipole magnetic field) that is invariant in azimuth for which the 2-D normal mode theory identifies the site of resonant coupling unambiguously: it must lie on a circle where the frequency of the toroidal Alfvén wave (i.e., that with azimuthal velocity and magnetic field perturbations) matches the driving frequency (ω_d). Thus, we know the permitted location of the resonance and the polarization given only ω_d. The sites on the dawn and dusk flanks where FLRs are most frequently observed are shown in red.

How does this differ in 3-D? Figure 1b shows that a magnetosphere with flared flanks is clearly not axisymmetric and so represents a fully 3-D medium. The red lines again indicate the typical location of the FLRs as found in simulations by *Claudepierre et al.* [2009, 2010] and *Degeling et al.* [2010]. The Alfvén frequencies of the toroidal and poloidal Alfvén waves have been studied extensively, and it is well known that they are different (particularly for the lower harmonics). Since the velocity and magnetic field of the Alfvén wave will lie along the resonant ridge [*Wright and Elsden*, 2016], the waves in Figure 1b cannot be simply toroidal or poloidal—so what will their frequency be for an intermediate polarization?

Degeling et al. [2010] show how progress can be made by considering the counterparts of both the poloidal and toroidal modes in more general coordinate systems. An alternative way to find the frequencies is to adopt the formalism of *Singer et al.* [1981] and adapt it for waves with polarization directed along the resonant ridge. In this fashion *Wright and Elsden* [2016] show how the Alfvén frequency varies smoothly with polarization angle on a given field line. They also show how this provides an explanation for Figure 1b by considering the field line labeled p: if the driving frequency is known, and p is on the resonance, then there will be a unique polarization for which the Alfvén wave is resonant. This polarization direction (which coincides with the orientation of the ridge) can be followed to field line q. Once at q the medium is slightly different, and so the polarization angle (and orientation of the ridge) at q changes slightly from that at p. Repeating this mapping process allows the resonant ridge to be traced out as shown.

However, it is also possible to start at a neighboring field line (p′) where the resonant polarization will be slightly different to that at p. Following the polarization direction at p′ to q′ a new ridge is mapped out (red dashed line). *Wright and Elsden* [2016] show how there is a Resonant Zone where an infinite family of these allowable solutions exist. In this sense 3-D FLRs are fundamentally different to those in 1-D and 2-D. They also identify factors that will favor one solution over another in a given situation. For the FLRs in a flared flank waveguide the favored ridge is the one that, when mapped to the subsolar point, will have a toroidal polarization. These predictions agree with the location and polarization of the Alfvén resonances found in the simulation results of *Claudepierre et al.* [2009, 2010], *Degeling et al.* [2010], and *Wright and Elsden* [2016]. See the latter publication for a more extensive discussion of their theoretical framework.

The aim of this paper is to extend the normal mode results of *Wright and Elsden* [2016] to the time-dependent regime. Time dependence gives causality to their results and permits the study of the formation of the resonance, along with associated effects such as phase mixing. We also provide (and validate) expressions for the width and amplitude of 3-D FLRs. The paper is laid out as follows: Section 2 discusses the model employed and the computational formulation; section 3 presents the key simulation results and analysis; and concluding remarks are made in section 4.

2. Model

While our modeling is directly relevant to FLRs in the Earth's magnetosphere, the focus of the present study is to provide a clear understanding of the processes involved in 3-D FLR formation, not to directly model any

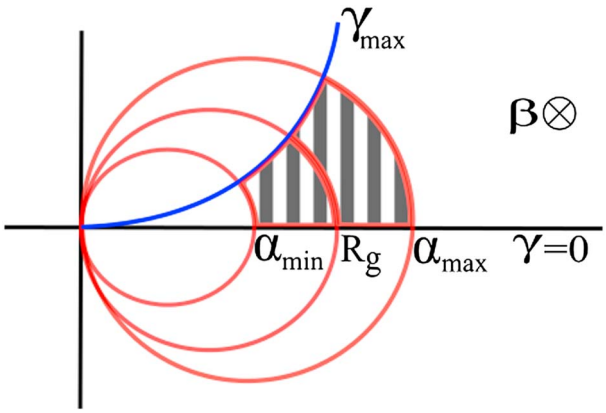

Figure 2. Schematic of 2-D dipole coordinate system. Lines of constant α are drawn in red, which represent magnetic field lines. Lines of constant γ are drawn in blue, where γ acts as a field-aligned coordinate. The shaded region bounded by the lines labeled α_{min}, α_{max}, $\gamma = 0$ and γ_{max} represents a possible simulation domain.

specific observations. A key aspect to elucidate arises from the toroidal and poloidal Alfvén eigenfrequencies being different and the necessity to understand waves with an intermediate polarization. To facilitate this aim, we do not choose an equilibrium that is intended to be an accurate representation of the magnetosphere. Rather we choose one that will allow the clearest identification of the physics in operation. To this end, we employ a 2-D magnetic dipole (rather than 3-D) as the fundamental Alfvén frequencies can differ by a factor of 3 (compared to 40% for a 3-D dipole).

2.1. Model Coordinates

We begin by briefly describing the field-aligned dipole coordinate system adopted in this paper. Full details can be found in *Wright and Elsden* [2016]. The system geometry is characterized by scale factors (h_α, h_β, h_γ) which are related to an element of real space $d\mathbf{r}$ by

$$d\mathbf{r} = \mathbf{e}_\alpha h_\alpha d\alpha + \mathbf{e}_\beta h_\beta d\beta + \mathbf{e}_\gamma h_\gamma d\gamma. \tag{1}$$

The problem inherent to the standard dipole coordinates [see for example *Kageyama et al.*, 2006] is that equal increments in a coordinate direction produce vastly different increments in path length, which creates computational difficulties. We therefore adopt a set of coordinates (α, β, γ) based on the 2-D dipole geometry. These, and the corresponding scale factors, are

$$\alpha = \frac{R}{\cos\phi}, \tag{2}$$

$$\beta = z, \tag{3}$$

$$\gamma = R_g \tan^{-1}\left(\frac{R_g}{R}\sin\phi\right), \tag{4}$$

$$h_\alpha = \cos^2\phi = \frac{1}{1+\Lambda^2}, \tag{5}$$

$$h_\beta = 1, \tag{6}$$

$$h_\gamma = \left(\frac{R}{R_g}\right)^2 + \sin^2\phi = \frac{1}{1+\Lambda^2}\left(\frac{\alpha^2}{R_g^2} + \Lambda^2\right), \tag{7}$$

where Λ is defined by

$$\Lambda(\alpha,\gamma) = \frac{\alpha}{R_g}\tan\left(\frac{\gamma}{R_g}\right). \tag{8}$$

(R, ϕ, z) are the standard cylindrical coordinates, and R_g is the radial equatorial crossing point of a field line, normally chosen in the center of the domain. The scale factors in (5)–(7) have also been defined in terms of the coordinates (α, β, γ), for use in defining the equations in the next section. A schematic of the coordinates is shown in Figure 2, with the striped region indicating a possible simulation domain.

2.2. MHD Equations

Now that the coordinates have been determined, we consider the formulation of the MHD equations in this system. *Wright* [1992] (equations (7) and (8) therein) states the linearized ideal MHD equations in a cold

plasma in general field-aligned orthogonal curvilinear coordinates. For the geometry described in the previous section, these equations become

$$\frac{\partial U_\alpha}{\partial t} = V_A^2 \frac{\left(1+\Lambda^2\right)^2}{\alpha^2/R_g^2+\Lambda^2}\left[\frac{\partial B_\alpha}{\partial \gamma} - \frac{\partial B_\gamma}{\partial \alpha}\right] - \nu U_\alpha, \tag{9}$$

$$\frac{\partial U_\beta}{\partial t} = V_A^2 \frac{1}{\alpha^2/R_g^2+\Lambda^2}\left[\frac{\partial B_\beta}{\partial \gamma} - \frac{\partial B_\gamma}{\partial \beta}\right] - \nu U_\beta, \tag{10}$$

$$\frac{\partial B_\alpha}{\partial t} = \frac{1}{\alpha^2/R_g^2+\Lambda^2}\frac{\partial U_\alpha}{\partial \gamma}, \tag{11}$$

$$\frac{\partial B_\beta}{\partial t} = \frac{\left(1+\Lambda^2\right)^2}{\alpha^2/R_g^2+\Lambda^2}\frac{\partial U_\beta}{\partial \gamma}, \tag{12}$$

$$\frac{\partial B_\gamma}{\partial t} = -\left(\frac{\alpha^2}{R_g^2}+\Lambda^2\right)\left[\frac{\partial U_\alpha}{\partial \alpha} + \frac{\partial U_\beta}{\partial \beta}\right]. \tag{13}$$

We have introduced the variables $U_\alpha = u_\alpha h_\beta B$, $U_\beta = u_\beta h_\alpha B$, $B_\alpha = b_\alpha h_\alpha$, $B_\beta = b_\beta h_\beta$, and $B_\gamma = b_\gamma h_\gamma$, in terms of the velocity (**u**) and magnetic field (**b**) perturbations, respectively, for computational efficiency. B is the background magnetic field strength, V_A the background Alfvén speed ($B/\sqrt{\mu_0\rho}$), and ν represents the strength of a linear drag term that has been added to the equation of motion to preclude a singularity developing. Alternate forms of dissipation could be added, such as viscosity, resistivity, or dissipative boundaries. The singularity can also be removed by driving the system with a frequency that has a small imaginary part. The structure of the resonance is surprisingly insensitive to the exact form of dissipation [*Wright and Allan*, 1996], and we consider the limit of small dissipation, so the drag is only significant at the resonance. We have normalized the equations by characteristic values: lengths by R_0; magnetic field by the background field $B_0 = B(R=R_0, \phi=0)$, densities by $\rho_0 = \rho(R_0, 0)$, velocities by $V_0 = B_0/\sqrt{\mu_0\rho_0}$, and times by $t_0 = R_0/V_0$.

2.3. Numerical Model and Domain Setup

To solve the system given by equations (9)–(13) numerically, we employ the leapfrog-trapezoidal finite difference scheme which is second-order accurate in time and space. For more details on this method, see *Zalesak* [1979]. We implement a staggered grid, where different variables are defined on different grids, which aids with the definition of derivatives.

The solution domain is indicated by the striped region in Figure 2. As shown, only the Northern Hemisphere is solved for to save on computational resources, with a symmetry condition imposed in the equatorial plane, such that the full solution corresponds to a fundamental mode over $-\gamma_{max} < \gamma < \gamma_{max}$. This is realized by setting nodes of velocity at the ionospheric end of the field lines ($\gamma = \gamma_{max}$), with antinodes at the equator ($\gamma = 0$). The inner boundary in α (α_{min}) is assumed to be perfectly reflecting (node of u_α), while the outer boundary (α_{max}) is driven with perturbations of b_γ to model driving by magnetic pressure. Driving in such a way has been demonstrated to simulate a node of b_γ at the outer boundary [*Elsden and Wright*, 2015], which lowers the fundamental radial mode to a quarter wavelength. The form of the driver is simply a running sinusoidal wave packet which is tailored to smoothly enter and exit the domain. The frequency of the driven signal is controlled by the phase speed of the packet and the wavelength in the β direction. We choose to have a relatively long wavelength driver to reduce the evanescence of the fast-mode incident on the domain. This will allow the most effective driving of resonances far from the driven boundary. Either side of the section of the domain where we study 3-D FLRs, we introduce additional dissipative buffer zones in the β coordinate. These act to dissipate any perturbations such that they do not return to the domain of interest.

The Alfvén speed profile is critical in providing a variation of the natural Alfvén frequency within the domain. Since there is no variation in β of the equilibrium magnetic field, the dependence on β in the system, and

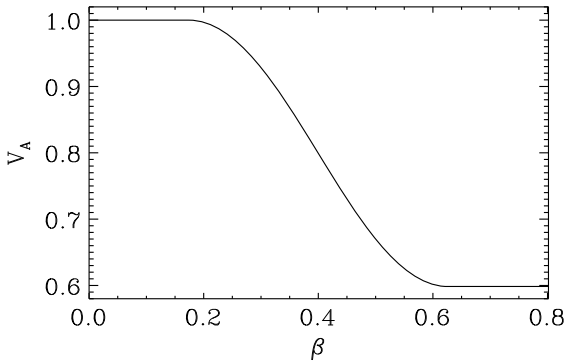

Figure 3. Variation of the Alfvén speed with β.

hence its 3-D inhomogeneous nature, is borne by the Alfvén speed profile. We impose a variation of the Alfvén speed, V_A, with β given by

$$V_A(\beta) = \begin{cases} 1 & 0 \le \beta \le \beta_{V_{A1}}, \\ 1 - \delta_{V_A} \sin^2 \left[\frac{\pi}{2} \left(\frac{\beta - \beta_{V_{A1}}}{\beta_{V_{A2}} - \beta_{V_{A1}}} \right) \right] & \beta_{V_{A1}} < \beta < \beta_{V_{A2}}, \\ 1 - \delta_{V_A} & \beta \ge \beta_{V_{A2}}, \end{cases} \tag{14}$$

where $\beta_{V_{A1}}$ and $\beta_{V_{A2}}$ define the different sections of the profile, and δ_{V_A} controls the change in V_A with β. Figure 3 displays the variation of V_A with β for the run discussed in this paper, with the specific values discussed in the next subsection. This shape has been specifically chosen to have uniform V_A regions at either end of the waveguide in β. This will allow purely 2-D toroidal resonance structures to develop in these regions. A decrease in V_A with β in the middle section will imply the point where the Alfvén frequency matches the driving frequency will move inward toward shorter field lines. The question is what will the polarization of the Alfvén wave be between these two uniform regions, which is to say, what path will the resonance take? To help identify this, we have set up the simulation so the resonant path is approximately equally inclined to both the α and β directions in the equatorial plane.

In order to test the method, multiple runs of varying complexity have been performed, for example, setting all of the scale factors to 1 to reproduce Cartesian results, including and removing dissipation, beginning with an initial displacement in the domain without driving, and using a small weakly nonuniform domain. From these test runs we have established the validity of the code, with energy typically conserved to one part in 10^4.

2.4. Run Specifications

For clarity and ease of reference, in this subsection we list the specific properties of the simulation performed. The domain covers $\alpha : 0.6 \rightarrow 1.0, \beta : 0.0 \rightarrow 0.8, \gamma : 0.0 \rightarrow 0.56$, with 160, 240, and 60 points taken in each of the three directions, respectively. These were chosen appropriately to resolve the smallest scales appearing in the simulation. $R_g = 0.8$ corresponding to the middle of the domain in α. On the field line with $\alpha = R_g$ in the equatorial plane, $\gamma = R_g\phi = 0.56$ is the path length along the field line from the equator to the ionospheric end at $\gamma_{\max}$ (latitude of $\phi = 0.7$ radians or 40°).

The dissipation regions in β span from $\beta = 0.0 \rightarrow 0.15$ and $\beta = 0.65 \rightarrow 0.8$. The dissipation ramps up gently over these regions so as not to act like a reflecting boundary and has a peak value of $\nu = 1.0$. The interior dissipation (from $\beta = 0.15 \rightarrow 0.65$) is set to $\nu = 0.1$. The driving frequency is chosen, in dimensionless units, as $\omega_d = 2.596$ (period $\tau = 2.420$), which is enforced by having a wavelength on the driven boundary of $\lambda_\beta = 10$ and a phase speed of $v_{\text{ph}} = 4.1317$. This frequency is tailored to excite resonances in the 2-D sections at desired locations in α, namely $\alpha = 0.65$ and $\alpha = 0.9$, for the Alfvén speed profile given in Figure 3. This is achieved by setting $\beta_{V_{A1}} = 0.175$, $\beta_{V_{A2}} = 0.625$, and $\delta_{V_A} = 0.40234$ in equation (14). The simulation is run for many decay times ($1/\nu$, for $\nu = 0.1$), in order to ensure a steady state is reached. A time step is chosen such that the CFL condition is comfortably satisfied everywhere.

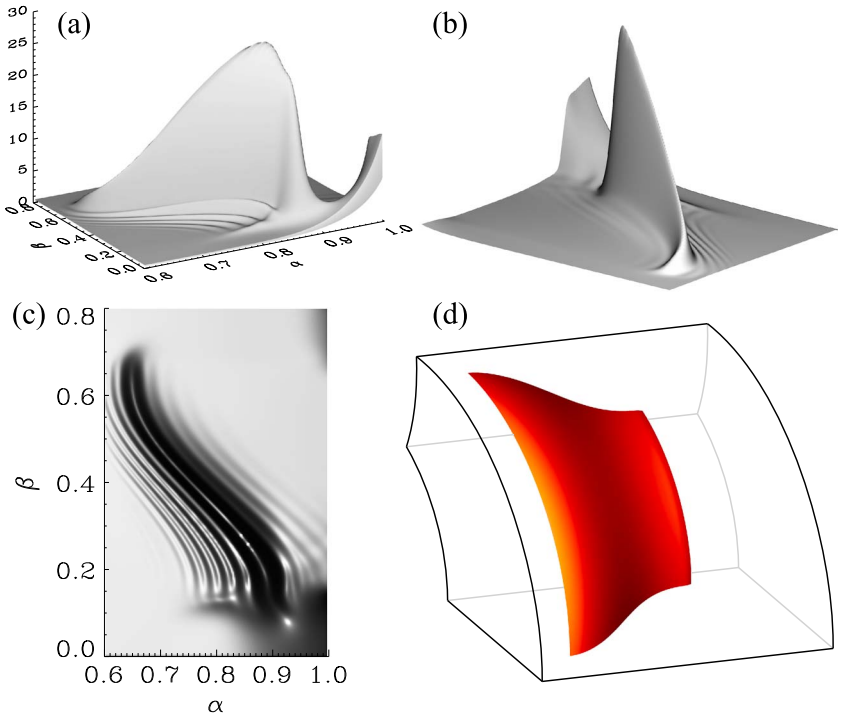

Figure 4. (a) Shaded surface plot of the flux tube energy density (FTED) at time $t = 46.89$, plotted in (α, β) coordinates. (b) Same as Figure 4a but from a rotated view. (c) Aerial view of the FTED at the same time. (d) A skeleton of the solution domain in physical space (black and grey lines), together with the resonant field lines mapped into physical space, which form a resonant sheet in 3-D.

3. Results

To most clearly display the structure of the resonance formed, we consider the total energy integrated along a field line in γ. This represents the energy density of a flux tube of unit cross section in the equatorial plane, and thus we refer to it as the flux tube energy density or FTED. This quantity captures the total energy in the Alfvén wave on a given flux tube, even though it travels back and forth along the tube throughout the wave cycle. It will also contain some fast-mode contributions, but these should not be too important at the resonance. We consider the FTED as an indicator of the location of the Alfvén resonance, since the resonance should manifest itself as a localized accumulation of energy.

Figure 4a displays a shaded surface plot of the FTED at time $t = 46.89$, while Figure 4b shows the same surface but from a reverse angle. There is a clear "resonant surface" formed, together with ridges which are more prominent on the inner (low α) side of the surface peak. The evanescent structure of the fast mode is clearly demonstrated by the decaying structure at the right-hand edge of Figure 4a, which is the driven side of the domain (at $\alpha = 1.0$). Figure 4c gives an aerial view of the FTED at the same time as Figures 4a and 4b. This highlights the structure of the resonant path in the (α, β) plane, as well as the presence of the ridges, which converge from the lower end of the resonance ($\beta \sim 0.15$) to the upper end ($\beta \sim 0.6$). Another feature highlighted here is the locally 2-D resonant regions, at $\alpha \sim 0.65$, $\beta \gtrsim 0.6$, and $\alpha \sim 0.9$, $\beta \lesssim 0.2$, which were tailored through the choice of the Alfvén speed profile. Figure 4d displays a skeleton of the solution domain in real space. Within this skeleton lies the physical surface formed of resonant field lines, colored red.

Figure 5a shows a shaded surface plot of the FTED at a time of $t = 117.24$, near to the end of the simulation. By this time, the domain has been steadily driven for many cycles. The ridges present at the earlier time have almost entirely decayed, as is made clear by the aerial view of the FTED at this time shown in Figure 5b. The location of the resonant ridge is unchanged from the previous time. It is also worth noting here that the resonance position does not vary along the field line in the γ direction, which is demonstrated for the steady state case by *Wright and Elsden* [2016]. They also demonstrated that the velocity and magnetic field perturbations are directed along the resonant ridge in real space, i.e., the wave fields are polarized along the resonance. Hence, it is possible to infer the path of the resonance from the FTED.

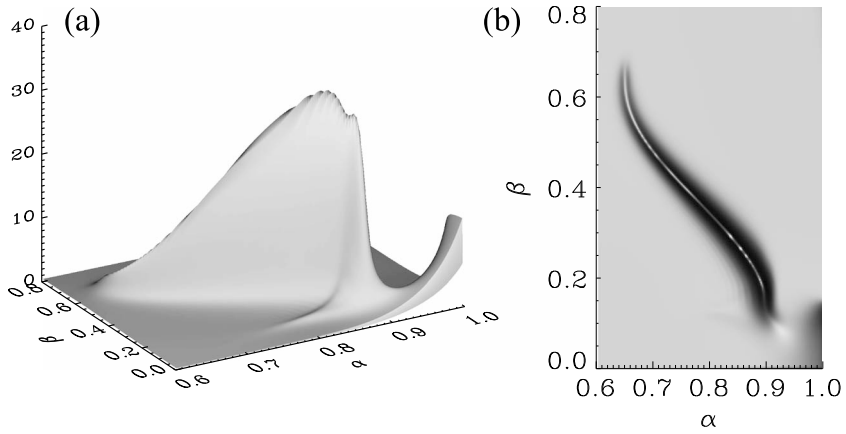

Figure 5. (a) Shaded surface of the FTED at a later time, $t = 117.24$. (b) Aerial view of Figure 5a.

Figures 4 and 5 raise many interesting questions about the structure of 3-D FLRs, which we address in this section. Such questions are as follows: What is the cause of the ridges in energy density (Figure 4c) and why do they decay in time? What determines the path taken by the resonance? How important is the difference between the poloidal and toroidal Alfvén eigenfrequencies? What theories can be applied from previous analytic approaches to describe properties of the resonance, for example, the amplitude and width?

3.1. Solutions to the Alfvén Wave Equation

We begin our analysis by explaining the path of the resonance. From the shaded surface plots of the previous section, we hypothesize that the accumulation of energy along a particular line in (α, β) space is due to the fast-driving frequency matching the Alfvén frequency. To show that this is indeed the case, we can solve the Alfvén wave equation along a field line at a location in (α, β). A thorough description of this process is given in the analysis of *Wright and Elsden* [2016] sections 4.1 and 4.2, which will be summarized here. We adapt the formulation for the Alfvén frequency in a curvilinear system given by *Singer et al.* [1981] by introducing a local coordinate system (α', β') aligned with the resonant contour. The Alfvén frequency depends upon the location and the polarization of the Alfvén wave, and we denote the latter by the angle θ that the Alfvén perturbations make to the β axis. Thus, we can express the Alfvén frequency as a function of its location and angle as $\omega_A = \omega_A(\alpha, \beta, \theta)$. Taking β' to be along the resonant contour, *Wright and Elsden* [2016] have shown that the appropriate scale factors on a given field line (along γ) are

$$h_{\alpha'} = \frac{h_\alpha(\gamma) h_\beta(\gamma)}{h_{\beta'}(\gamma_0)} \sqrt{\frac{h_\alpha^2(\gamma_0)\sin^2\theta + h_\beta^2(\gamma_0)\cos^2\theta}{h_\alpha^2(\gamma)\sin^2\theta + h_\beta^2(\gamma)\cos^2\theta}}, \tag{15}$$

$$h_{\beta'} = h_{\beta'}(\gamma_0) \sqrt{\frac{h_\alpha^2(\gamma)\sin^2\theta + h_\beta^2(\gamma)\cos^2\theta}{h_\alpha^2(\gamma_0)\sin^2\theta + h_\beta^2(\gamma_0)\cos^2\theta}}, \tag{16}$$

where h_α and h_β are as previously defined by equations (5) and (6), and γ_0 is the minimum in γ, which in our case is $\gamma_0 = 0$ (note that $h_\alpha(\gamma)$ is a shorthand notation for $h_\alpha(\alpha, \beta, \gamma)$ on the chosen field line (α, β)). Given these scale factors, we can state the Alfvén wave equation for an arbitrary polarization angle as [*Wright and Elsden*, 2016]

$$\frac{\partial}{\partial\gamma}\left(\frac{1}{h_\gamma}\frac{\partial U_{\beta'}}{\partial\gamma}\right) + \frac{1}{h_\gamma}\frac{\partial}{\partial\gamma}\left(\ln\left(\frac{h_{\beta'}}{h_{\alpha'}}\right)\right)\frac{\partial U_{\beta'}}{\partial\gamma} + \frac{\omega_A^2}{V_A^2} h_\gamma U_{\beta'} = 0. \tag{17}$$

This formulation is based upon the Alfvén wave operators derived by *Wright and Thompson* [1994] for the separate Alfvén wave polarizations (poloidal and toroidal). Setting $\theta = 0$ (toroidal) or $\theta = \pi/2$ (poloidal) recovers these equations. Equation (17) can be solved at a given position and polarization angle to yield the natural Alfvén frequency. We can therefore use a shooting code to search for, at each location (α, β), the angle θ such that the Alfvén frequency matches the imposed driving frequency. Such an angle will not necessarily exist,

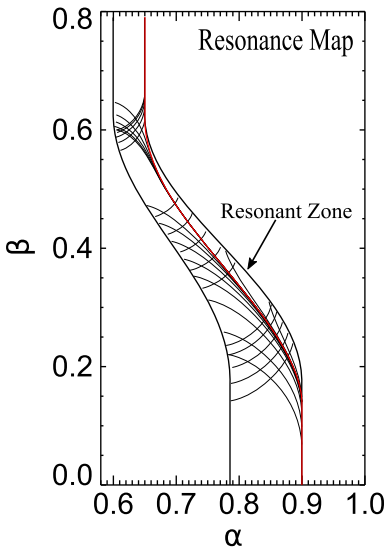

Figure 6. The Resonance Map for the numerical simulation, which represents permissible solutions to equations (17) and (18). Selected contours have been drawn.

which is discussed in detail by *Wright and Elsden* [2016], and there will be a Resonant Zone where solutions do exist. Since the orientation of the resonant contour in the (α, β) plane has a slope of θ, it follows that

$$\frac{\mathrm{d}\alpha}{\mathrm{d}\beta} = \tan\theta. \tag{18}$$

Hence, for a starting position say (α_0, β_0), we can solve equation (17) to find the correct θ such that the Alfvén frequency equals the fast-mode frequency. Then equation (18) can be solved using a simple Euler method to step along the contour. In this way, resonant contours can be traced throughout the Resonant Zone in the (α, β) plane, which will form what we call a Resonance Map [*Wright and Elsden*, 2016], shown for the simulation in question in Figure 6. The Resonant Zone is bounded on the left by poloidal polarizations ($\theta = \pi/2$) and the right by toroidal ($\theta = 0$), as can be seen by the angle at which contours approach these lines. Various contours cross each other because both θ and $-\theta$ are valid solutions to equation (17).

What is immediately clear is the reproduction of the main resonant contour from the simulation (Figure 5b) as one of the family of permitted solutions in the Resonance Map. This confirms the original hypothesis that this contour is indeed resonant and represents a matching of the Alfvén and fast-mode frequencies. To be clear, along all of the contours plotted in Figure 6, the Alfvén frequency matches the driving frequency. So why do we only see one as dominant in the simulation? *Wright and Elsden* [2016] have shown that there are a few mechanisms by which different contours can be favored over others, such as boundary conditions which favor a particular polarization of the Alfvén wave, or locally 2-D resonant regions which have a similar effect. Their theory identifies the contour originating from the 2-D region at $\beta > 0.6$ as being favored and is shown in red in Figure 6. Indeed, this particular solution matches very well with the ridge in Figure 5b.

The shape of the resonant ridges is governed predominantly by the Alfvén speed profile. *Lee et al.* [2000] found similar behavior, where they observed dominant oscillations tangential to surfaces of constant Alfvén speed. The authors considered a Cartesian geometry with an asymmetric Alfvén speed profile. This means they lacked the differing toroidal and poloidal frequencies which further influence the possible Alfvén wave polarization. However, they still captured the way in which the asymmetry of V_A affected the resonance location throughout the domain. Similar features were also discussed by *Russell and Wright* [2010].

It is worth highlighting further the importance of differing poloidal and toroidal Alfvén eigenfrequencies. If these frequencies were the same, as is the case in a Cartesian geometry with $h_\alpha = h_\beta = 1$, the idea of a Resonant Zone of solutions no longer exists, and the bounds of the toroidal and poloidal frequencies in Figure 6 collapse onto one another. This highlights the difference between this work and that of *Russell and Wright* [2010] and *Lee et al.* [2000]. If it were computationally feasible to extend the domain in γ to higher latitudes, the disparity would grow between the two modes, which would result in a broader Resonant Zone in the Resonance Map.

3.2. Resonant Ridges—Natural Frequencies

We now consider the ridges in energy density apparent at early times in the simulation (e.g., Figure 4c). The fact that these features decay in time leads to the thought that they represent a natural response of the system to the imposed driving, which decays due to the dissipation ν. At early times, before the system has been driven for many cycles, regions where the natural Alfvén frequency is close to the driven frequency may also be excited. To investigate this, we performed an ideal ($\nu = 0$) simulation with all other parameters unchanged. Being ideal, the natural responses will not decay and hence are easier to detect.

Figure 7a plots the time series for U_β (from this $\nu = 0$ simulation) at a point close to the center of the main resonant ridge, with the corresponding fast Fourier transform (FFT) power plotted in Figure 7b. This reveals the driving frequency of $\omega_d = 2.596$ ($f_d = 0.41$) to be dominant, with no other frequencies present, which is as expected since the Alfvén and fast frequencies coincide here. Figure 7c again displays the time series for U_β

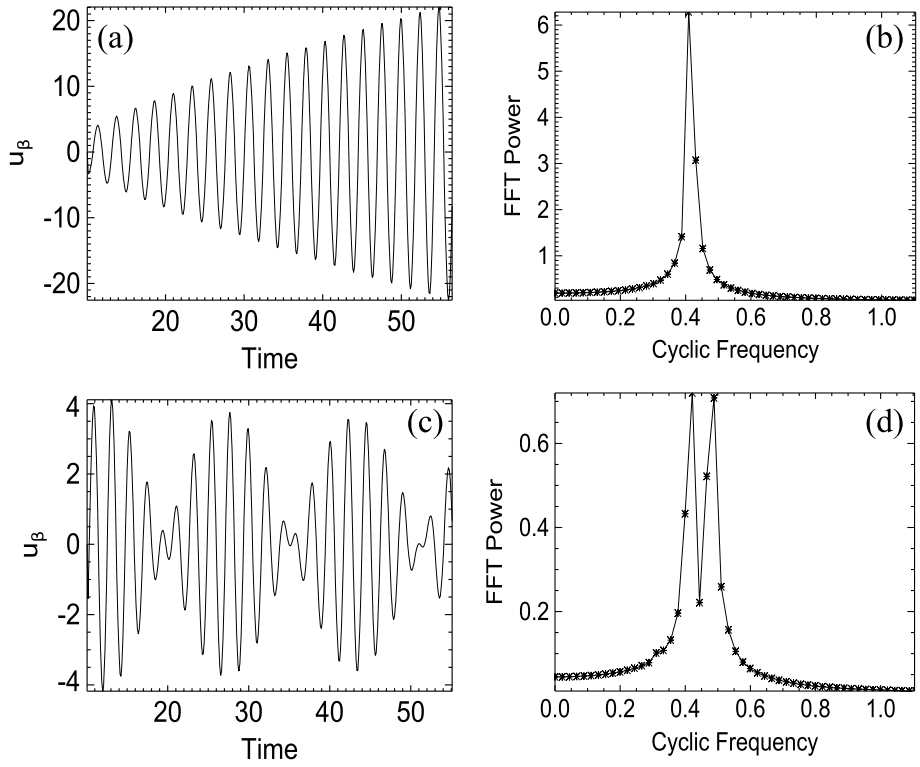

Figure 7. (a) Time series for U_β from a point on the main resonant line. (b) FFT for time series in Figure 7a. (c) Time series for U_β at a location off the main resonant line. (d) FFT for time series in Figure 7c.

except now from a point just off the main resonant contour, with its FFT plotted in Figure 7d. As the beating profile suggests, there are two frequencies present. One is clearly the driving frequency. To investigate the second frequency, similar plots to those in Figure 7 (not shown here) were produced for different locations. When the field lines lie on the same ridge, the same two frequencies are observed. Moreover, as the ridges are crossed, the second frequency varies systematically, as shown in Figure 8a. Similar results have been observed in the nonlinear simulations of Alfvén resonances detailed in Figure 12 of *Terradas et al.* [2016].

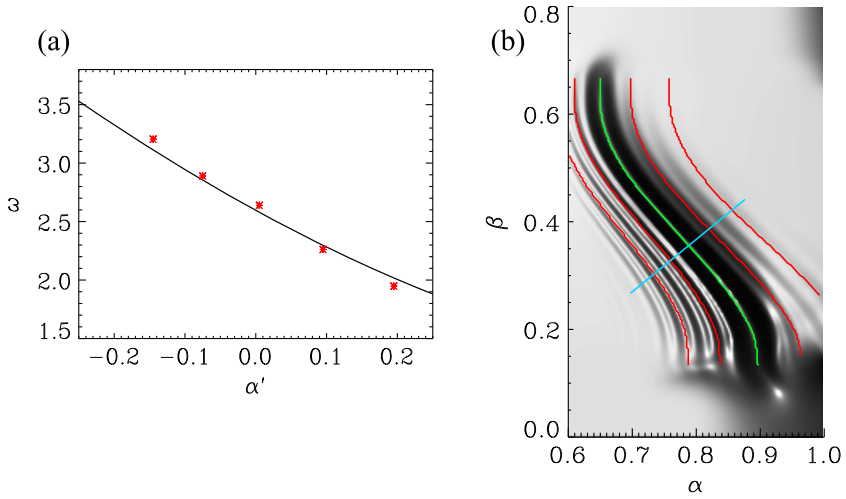

Figure 8. (a) A plot of the observed natural Alfvén frequency versus α' (symbols) and the value estimated from equation (17) (line). (b) Shaded surface plot of the FTED as in Figure 4c, with the red ridges representing the location of the main resonant contour from steady state simulations with driving frequencies from left to right of $\omega_d = [2.010, 2.303, 2.889, 3.182]$. The green line is for the case matching the driving frequency of $\omega_d = 2.596$. The blue line represents a slice in the α' direction, along which the frequencies are measured in Figure 8a.

The coordinate α' corresponds to the distance (in the equatorial plane) from the resonant ridge, along the cut shown in Figure 8b as the blue line. The green line denotes the center of the resonant ridge. Figure 8a shows the nondriven frequency from the FFT as red symbols. Also plotted (as the solid line) is the field line Alfvén frequency predicted from equation (17). The agreement clearly indicates that the second frequency we observe is a free oscillation of the field line at its natural Alfvén frequency.

It is instructive to think of the whole solution as a Fourier summation over frequency. The normal modes calculated in *Wright and Elsden* [2016] correspond exactly to these, so we could think of the time-dependent results of our simulations as corresponding to a suitable sum of their normal modes. Evidently, those modes with frequencies close to the driven frequency will make a significant contribution. For example, calculating the normal mode for $\omega = 2.303$ provides an accumulation of energy along the ridge shown by the red line just to the right of the green line in Figure 8b. This, not surprisingly, corresponds exactly with the ridge in our time-dependent simulation where the natural Alfvén frequency matches that of the normal mode. Similar agreement is found for other normal modes with frequencies around ω_d (indicated by the other red lines in Figure 8b). The fact that these features represent a free Alfvén oscillation accounts for their absence at later times when dissipation is included. These features are clearly the 3-D manifestation of phase mixing, and we expect the phase mixing length to follow a similar form to that given in *Mann et al.* [1995], which in 3-D is

$$L_{\mathrm{ph}} = \frac{2\pi}{|\nabla\omega_A(\alpha',\beta',\theta)|t} = \frac{2\pi h_{\alpha'}}{|\partial\omega_A(\alpha',\beta',\theta)/\partial\alpha'|t}. \tag{19}$$

This accounts for the narrowing of scales with time (which is seen if Figure 8b is viewed as a movie in time) until the free oscillations decay. The phase motion of the ridges will be from high to low Alfvén frequency [*Wright et al.*, 1999].

Similar beating effects resulting from Alfvén wave phase mixing are seen in the simulations of *Poedts and Kerner* [1992], where a straight axisymmetric cylindrical equilibrium using resistive MHD was considered. At early times, energy accumulates in the region surrounding the location of the singularity [see e.g. Figure 5 *Poedts and Kerner*, 1992], which would become "ridges" in a 3-D system.

In a more realistic scenario, where the source is broadband not monochromatic, we would expect there to be multiple resonances in the domain. These resonances could overlap, significantly enough to preclude appearance of the natural frequency (off resonant) responses that we have termed ridges. This is something that we will consider in future work and certainly will have to be considered for any application to observations. However, it is important at this stage to understand the most basic behavior first.

3.3. Resonance Widths—Temporal Dependence

Having generated a FLR in 3-D, one of the basic properties to consider is the resonance width, which is physically important to understand how localized the energy accumulation is in space. Initially, the width is governed by the phase mixing length (as mentioned above), which determines the smallest scales appearing in the domain. Phase mixing is the process by which neighboring field lines drift out of phase over time, due to the inhomogeneous background Alfvén frequency [*Burghes et al.*, 1969; *Heyvaerts and Priest*, 1983], which creates steep gradients in space. Dissipation limits the phase mixing length, such that the scales do not decrease indefinitely. It is of interest to see how the widths measured from the 3-D simulation compare to theoretical estimates from 1-D theory. First, we consider the evolution of the resonance width in time at a particular location along the main resonant contour.

The formula in equation (19) can be used to estimate the early width of the resonance before it is limited by dissipation. A more general calculation, valid for any stage in the resonance development, also exists. We follow the temporal width procedure of *Mann et al.* [1995], which involves considering the spectral power of the fast-mode driver. The spectral power at a time τ_0 can be expressed as (compare to *Mann et al.* [1995] equation (14)])

$$P(\omega) = \frac{1 + e^{-2\omega_i\tau_0} - 2e^{-\omega_i\tau_0}\cos\left[(\omega_r - \omega)\tau_0\right]}{\left[\omega_i^2 + (\omega_r - \omega)^2\right]}, \tag{20}$$

where ω_r and ω_i are the real and imaginary components of the fast-mode driving frequency. The resonance width will depend upon the frequency bandwidth of $P(\omega)$, and we denote the full width at half maximum

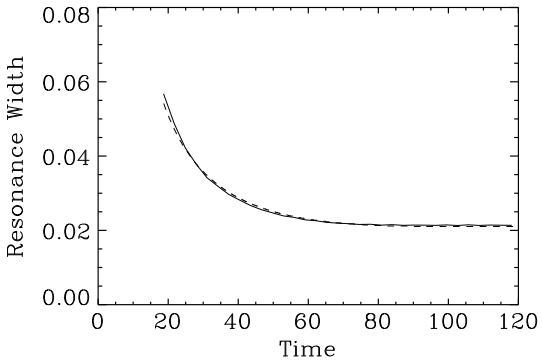

Figure 9. Temporal dependence of the resonance width at ($\alpha = 0.831$, $\beta = 0.294$) on the main resonant contour. The solid line is the measured simulation width, and the dashed line is the estimate.

(FWHM) of this profile at time τ_0 by $\Delta\omega(\tau_0)$. *Mann et al.* [1995] show that an estimate of the spatial width of the resonance at time τ_0, $\Delta X(\tau_0)$, can be found by the relation

$$\Delta X(\tau_0) = \frac{\Delta\omega(\tau_0)}{\omega_A'}, \tag{21}$$

where ω_A' is the Alfvén frequency gradient at the location in question.

To investigate the change of the resonance width in time, we performed a new simulation, where the boundary not only was driven with a real frequency but also had an amplitude that grew in time exponentially. This is in exactly the same fashion one would find by taking the real part of $\exp(-i\omega_d t)$ with a suitable complex ω_d. The results from this were essentially the same, regarding the resonance widths, as simulations where ω_d is real but dissipation is included. Equation (21) for the resonance width requires the Alfvén frequency gradient. We find this by considering the change of the Alfvén frequency perpendicular to the resonant contour, which in our coordinates aligned with the resonant ridge discussed in section 3.1, is the α' direction. To compare the estimate to the simulation, we choose a point along the main resonance and measure the FWHM of $u^2_{\beta'}$ in α' over time. This quantity represents the square of the physical velocity perturbation parallel to the resonant contour, which will be dominated by the Alfvén wave contribution. There is a periodic variation in the width coinciding with the period of the driver, and hence the time averaged width (over one period) is used. Figure 9 plots the time averaged estimate of the width using the above formulation as the dashed line, together with the width measured from the simulation as the solid line, for a point on the resonance. The agreement is excellent, which shows that the Alfvén frequency gradient and the bandwidth of the driver are still the governing factors of the resonance width in 3-D. Furthermore, considering the frequency bandwidth of the driver clearly captures the narrowing of the width in time, as found by *Mann et al.* [1995]. It is also evident that the simulation has indeed reached the steady state, with the widths leveling out to a constant value at late times.

3.4. Resonance Widths—Steady State

Having considered the development of the resonance width in time, we now look at the change of the resonance width in space once the system has reached a steady state. Since the Alfvén frequency gradient changes over the domain, we expect the widths to do so as well by equation (21). Indeed, considering the convergence of the phase mixing ridges (contours of constant Alfvén frequency) in Figure 4c, one would expect a considerable change in the widths. For the original simulation presented in this paper (up to and including Figure 5), the interior dissipation was set at $\nu = 0.1$, which represented a case close to what could be computationally achieved when running to the steady state time. For the detailed analysis of the steady state width, however, we choose to simply solve for the steady state solution directly, as described in *Wright and Elsden* [2016]. The assumed temporal dependence is $\exp(i\omega t)$, where ω has an imaginary part of $\omega_i = 0.03$ and $\nu = 0$. As before, we measure the width from the simulation using the FWHM of $u^2_{\beta'}$. We trace the location of the resonant contour in α, β space using peaks in the energy density, and at several locations along the resonant ridge, we calculate the width of the resonance. This is plotted as a function of β as the dashed line in Figure 10, where the x axis

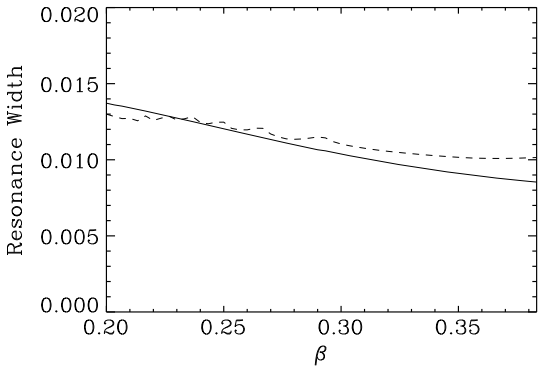

Figure 10. Variation of resonance width in the $\gamma = 0$ plane along the resonant ridge, parameterized in terms of β. Simulation width measurement is the dashed line, with the estimate in equation (22) as the solid line.

represents position on the resonant ridge, starting from the lower end in β, and is parameterized in terms of β. The entire contour is not plotted because at the innermost end (lower α region), the amplitude is not large enough to accurately measure the FWHM, and at the outermost end the fast mode contaminates the results.

The width estimate is formed using the late time limit of equation (21) ($\tau_0 \gg 1/\omega_i$). In this limit, $P(\omega)$ (from equation (20)) has a Lorentzian profile, with a FWHM of $\Delta\omega = 2\omega_i$. This then allows the resonance width in the steady state to be written as [*Southwood and Allan*, 1987]

$$\Delta X(\tau_0) = 2\omega_i(\omega'_A)^{-1}. \tag{22}$$

This estimate is plotted as the solid line in Figure 10. The estimate agrees well with the simulation values over the majority of the resonant contour (within 10%) but diverges toward the lower amplitude region. We believe this to be caused by a few factors: First, the width predictions are accurate only in the limit as $\omega_i \to 0$ ($\nu \to 0$), and thus, there will be a difference between the simulation and the estimate from using a value of $\omega_i = 0.03$. As previously mentioned, the accuracy of the FWHM measurement declines with decreasing amplitude. This is not helped by there being some fast-mode contributions to the resonance, which further skews the FWHM measurement. However, this result is still a very good comparison of theory with simulation and again demonstrates how the ideas of 1-D resonances cross over to the 3-D case presented here.

3.5. Resonance Amplitudes

A key area to investigate is the amplitude of the resonance. This is physically significant in determining how much energy can be accumulated locally in the resonant sheet. For example, in a magnetospheric setting, it is of paramount interest to understand how efficiently FLRs may be excited in 3-D, given that they represent regions where energy is propagated along the magnetic field and deposited into the ionosphere. Our simulation results have clearly demonstrated the formation of a resonance of significant amplitude in an inhomogeneous 3-D geometry. The amplitude in the outermost extended 2-D (toroidal only) resonant region at $\alpha \sim 0.9$ has a similar amplitude to parts of the 3-D resonant region. This shows that the efficiency of excitation of 2-D and 3-D resonances is similar. It had been postulated by *Inhester* [1986] that increasing asymmetry could reduce the strength of the mode coupling, but we do not find evidence for this based on our results.

In this section, as with the previous sections on resonance widths, we try to find analytical estimates for the resonance amplitude borrowed from previous 2-D theory and then compare these to the measured simulation amplitudes. The following analysis draws on results from *Russell and Wright* [2010] and *Wright and Thompson* [1994] and generalizes these to our situation in a plausible fashion. The former of these works considers a Cartesian system with an assumed steady state time dependence of $\exp(-i\omega t)$, where the density varies in both directions across the straight background field. The resulting equations are solved by a Frobenius method, which to leading order shows that the displacement along the resonance scales as the gradient of the field-aligned magnetic field perturbation, i.e., the magnetic pressure gradient. The work of *Wright and Thompson* [1994] considers a field-aligned curvilinear system, (α, β, γ), which can be compared to the system used in this paper. A harmonic dependence of $\exp\left(i\left(k_\beta\beta - \omega t\right)\right)$ (β being the azimuthal direction) is factored out of the equations, while the background density varies along and across the magnetic field. Again, a Frobenius solution was derived, which to leading order yielded relations for the b_γ (field-aligned magnetic field) and ξ_β (azimuthal displacement) perturbations (see equations (43) and (45a)–(45c) of *Wright and Thompson* [1994], for reference). We propose reinstating a general β dependence to extend this analysis to the 3-D scenario.

Using the coordinates (α', β') as discussed in section 3.1, such that $\alpha' = 0$ represents the location of the resonance, for a time dependence of $\exp(-i\omega t)$ we propose a solution to leading order of the following form that reduces to the 2-D results of *Wright and Thompson* [1994] and *Russell and Wright* [2010] when simplified appropriately.

$$b_\gamma(\alpha', \beta', \gamma) \simeq b_{\gamma_0}(0, \beta', \gamma), \tag{23}$$

$$\xi_{\beta'}(\alpha', \beta', \gamma) \simeq \frac{\beta_0}{\alpha'}\xi_{\beta'_A}(0, \beta', \gamma), \tag{24}$$

$$\beta_0 = \frac{1}{2\mu_0\omega_d}\frac{\left\langle Bh_{\alpha'}\xi_{\beta'_A}\partial\left(h_\gamma b_{\gamma_0}\right)/\partial\beta'\right\rangle_{(0,\beta')}}{\left\langle \rho\xi^2_{\beta'_A}h_{\alpha'}h_{\beta'}h_\gamma\right\rangle_{(0,\beta')}}\left(\frac{\mathrm{d}\omega_A}{\mathrm{d}\alpha'}\right)^{-1}_{(0,\beta')}. \tag{25}$$

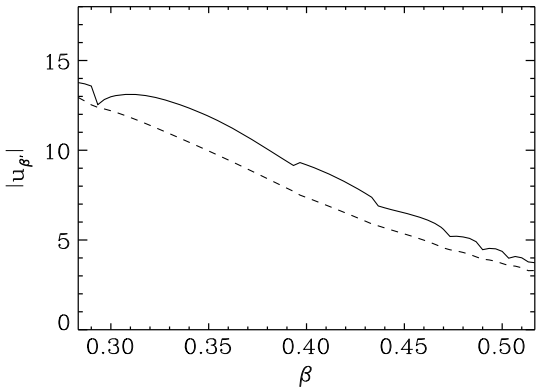

Figure 11. Amplitude of $u_{\beta'}$ plotted against β along the resonant contour. Amplitude from the simulation is the dashed line, and estimate is the solid line.

The terms appearing in the above equations are: b_{γ_0} is the leading order term of the Frobenius series solution for b_γ; ω_d is the fast-mode driving frequency; B is the background magnetic field; ρ is the background density; and $\xi_{\beta'_A}$ is the resonant Alfvén eigenfunction in the β' direction (i.e., a solution for the displacement to the Alfvén wave equation (17)). The angled brackets in equation (25) represent integration along the field line in γ at a location on the resonance denoted by $(0, \beta')$. Our goal here is to evaluate the expression for β_0 in equation (25) and to then calculate the amplitude of the displacement $\xi_{\beta'}$ in (24). The singularity occurs where $\omega_A = \omega_d$, and if ω_d is complex, this is not satisfied for a real location α but formally at a complex position

$$\alpha' = \alpha'_r + i\alpha'_i. \tag{26}$$

with the Alfvén frequency at $\alpha' = 0$ matching the real part of ω_d. In this formulation, α_i corresponds to the resonance half-width, which can be found from adapting equation (22) to give $2\alpha_i = 2\omega_i/(\mathrm{d}\omega_A/\mathrm{d}\alpha')$. We take the value for b_{γ_0} as the complex valued b_γ from the steady state simulation previously mentioned. The resonant eigenfunction $\xi_{\beta'_A}$ can be calculated at each point along the resonance by solving the Alfvén wave equation (17) using the shooting method discussed in section 3.1. The other quantities are all known, and we can thus evaluate the derivatives and integrals appearing in equation (25). From this follows the amplitude of $\xi_{\beta'}$ which can be calculated from equation (24). For ease of comparison with our simulation we consider the amplitude of $u_{\beta'}$, which can be found from $\xi_{\beta'}$ as

$$|u_{\beta'}| = \sqrt{\omega_d^2 + \omega_i^2}\,|\xi_{\beta'}|. \tag{27}$$

Figure 11 plots this amplitude measured from the simulation along a portion of the resonant contour as the dashed line. A steady decrease of amplitude as the resonant ridge is followed radially inward (to lower α) is also seen in the shaded surface plots of Figures 4 and 5. Using the above method, we form an estimate for $|u_{\beta'}|$ which is plotted in Figure 11 as the solid line. To form this estimate, the measured simulation resonance width is used. The analytical estimate and the simulation show good agreement along the contour. This is remarkable given that the estimate has been extended from 2-D theory in an ad hoc fashion and is not itself a full 3-D solution to the system. However, it shows that the dominant characteristics of the resonance amplitude remain similar in 3-D. In this manner, we have provided a useful estimate for the amplitude of a 3-D resonance in a field-aligned coordinate system.

4. Concluding Remarks

This paper has analyzed the time-dependent behavior of 3-D Alfvén resonances in a dipole geometry using the MHD equations under a low β assumption. This is an extension of the steady state system studied by *Wright and Elsden* [2016]. Through numerical simulations, we have shown the development of 3-D resonances and have discussed their characteristics. The main findings of this paper are as follows:

1. Resonances in 3-D can form over a Resonant Zone, in which the natural Alfvén frequency matches the driving frequency for some polarization of the Alfvén wave. There are a family of solutions, and the selection of the dominant resonant contour depends mainly upon the boundary conditions and the presence of locally 2-D toroidal resonant regions. This is a confirmation of the results of the steady state case [*Wright and Elsden*, 2016], extended to the time-dependent regime. The results presented here have found no contradictions to those from the steady state case.
2. Phase mixing is associated with beating at locations where the Alfvén frequency is close to the fast-driving frequency. This manifests in the time-dependent case as phase mixing ridges. The spacing of the ridges depends on the Alfvén frequency gradient and time early in the resonance evolution and is limited by dissipation for large times.

3. The resonance width decays in time in the 3-D case in exact accord with the 1-D theory of *Mann et al.* [1995]. This can be accurately analyzed using the frequency bandwidth of the driver, together with the Alfvén frequency gradient.
4. The steady state resonance width also shows good agreement with previous 1-D theory [e.g., *Southwood and Allan*, 1987; *Mann et al.*, 1995].
5. The resonance amplitude in 3-D can be modeled to a good approximation by an extension of the 2-D field-aligned curvilinear coordinate formulation of *Wright and Thompson* [1994]. Formulas for the resonance amplitude have been presented. We have shown that the amplitude of 3-D resonances is comparable to the standard 2-D toroidal resonance and thus have demonstrated that 3-D resonances can result in a significant local accumulation of energy.

Acknowledgments
Both authors were funded in part by STFC (through consolidated grant ST/N000609/1) and the Leverhulme Trust (through research grant RPG-2016-071). Data from simulation results are available upon request from T. Elsden, e-mail: te55@st-andrews.ac.uk.

References

Allan, W., S. P. White, and E. M. Poulter (1985), Magnetospheric coupling of hydromagnetic waves—Initial results, *Geophys. Res. Lett.*, *12*, 287–290, doi:10.1029/GL012i005p00287.

Allan, W., E. M. Poulter, and S. P. White (1986a), Hydromagnetic wave coupling in the magnetosphere—Plasmapause effects on impulse-excited resonances, *Planet. Space Sci.*, *34*, 1189–1200, doi:10.1016/0032-0633(86)90056-5.

Allan, W., S. P. White, and E. M. Poulter (1986b), Impulse-excited hydromagnetic cavity and field-line resonances in the magnetosphere, *Planet. Space Sci.*, *34*, 371–385, doi:10.1016/0032-0633(86)90144-3.

Burghes, D. N., P. C. Kendall, and P. A. Sweet (1969), A Physical explanation of difficulties appearing in the theory of toroidal magnetohydrodynamic oscillations, *Mon. Not. R. Astron. Soc.*, *143*, 9, doi:10.1093/mnras/143.1.9.

Chen, L., and A. Hasegawa (1974), A theory of long-period magnetic pulsations: 1. Steady state excitation of field line resonance, *J. Geophys. Res.*, *79*, 1024–1032, doi:10.1029/JA079i007p01024.

Claudepierre, S. G., M. Wiltberger, S. R. Elkington, W. Lotko, and M. K. Hudson (2009), Magnetospheric cavity modes driven by solar wind dynamic pressure fluctuations, *Geophys. Res. Lett.*, *36*, L13101, doi:10.1029/2009GL039045.

Claudepierre, S. G., M. K. Hudson, W. Lotko, J. G. Lyon, and R. E. Denton (2010), Solar wind driving of magnetospheric ULF waves: Field line resonances driven by dynamic pressure fluctuations, *J. Geophys. Res.*, *115*, A11202, doi:10.1029/2010JA015399.

Degeling, A. W., R. Rankin, K. Kabin, I. J. Rae, and F. R. Fenrich (2010), Modeling ULF waves in a compressed dipole magnetic field, *J. Geophys. Res.*, *115*, A10212, doi:10.1029/2010JA015410.

Dungey, J. (1954), Electrodynamics of the outer atmosphere: Report to National Science Foundation on work carried on under grant NSF-G450, *Sci. Rep.*, no. 69, The Pa. State Univ., Ionosphere Res. Lab.

Dungey, J. W. (1967), Hydromagnetic waves, in *Physics of Geomagnetic Phenomena*, edited by S. Matsushita and W. H. Campbell, p. 913, Academic Press, New York.

Elsden, T., and A. N. Wright (2015), The use of the Poynting vector in interpreting ULF waves in magnetospheric waveguides, *J. Geophys. Res. Space Physics*, *120*, 166–186, doi:10.1002/2014JA020748.

Heyvaerts, J., and E. R. Priest (1983), Coronal heating by phase-mixed shear Alfven waves, *Astron. Astrophys.*, *117*, 220–234.

Inhester, B. (1986), Resonance absorption of Alfven oscillations in a nonaxisymmetric magnetosphere, *J. Geophys. Res.*, *91*, 1509–1518, doi:10.1029/JA091iA02p01509.

Kageyama, A., T. Sugiyama, K. Watanabe, and T. Sato (2006), A note on the dipole coordinates, *Comput. Geosci.*, *32*, 265–269, doi:10.1016/j.cageo.2005.06.006.

Lee, D.-H., and R. L. Lysak (1989), Magnetospheric ULF wave coupling in the dipole model—The impulsive excitation, *J. Geophys. Res.*, *94*, 17,097–17,103, doi:10.1029/JA094iA12p17097.

Lee, D.-H., and R. L. Lysak (1990), Effects of azimuthal asymmetry on ULF waves in the dipole magnetosphere, *Geophys. Res. Lett.*, *17*, 53–56, doi:10.1029/GL017i001p00053.

Lee, D.-H., R. L. Lysak, and Y. Song (2000), Field line resonances in a nonaxisymmetric magnetic field, *J. Geophys. Res.*, *105*, 10,703–10,712, doi:10.1029/1999JA000295.

Mann, I. R., A. N. Wright, and P. S. Cally (1995), Coupling of magnetospheric cavity modes to field line resonances: A study of resonance widths, *J. Geophys. Res.*, *100*, 19,441–19,456, doi:10.1029/95JA00820.

Poedts, S., and W. Kerner (1992), Time scales and efficiency of resonant absorption in periodically driven resistive plasmas, *J. Plasma Phys.*, *47*, 139–162, doi:10.1017/S0022377800024120.

Russell, A. J. B., and A. N. Wright (2010), Resonant absorption with 2-D variation of field line eigenfrequencies, *Astron. Astrophys.*, *511*, A17, doi:10.1051/0004-6361/200912669.

Singer, H. J., D. J. Southwood, R. J. Walker, and M. G. Kivelson (1981), Alfven wave resonances in a realistic magnetospheric magnetic field geometry, *J. Geophys. Res.*, *86*, 4589–4596, doi:10.1029/JA086iA06p04589.

Southwood, D. J. (1974), Some features of field line resonances in the magnetosphere, *Planet. Space Sci.*, *22*, 483–491, doi:10.1016/0032-0633(74)90078-6.

Southwood, D. J., and W. Allan (1987), Hydromagnetic cavity eigenmodes in a non-uniform plasma, in *Small Scale Plasma Processes in the Solar Chromosphere/Corona, Interplanetary Medium and Planetary Magnetospheres*, edited by B. Battrick and E. J. Rolfe, *ESA Spec. Publ. 275*, 179–184.

Southwood, D. J., and M. G. Kivelson (1986), The effect of parallel inhomogeneity on magnetospheric hydromagnetic wave coupling, *J. Geophys. Res.*, *91*, 6871–6876, doi:10.1029/JA091iA06p06871.

Terradas, J., R. Soler, M. Luna, R. Oliver, J. L. Ballester, and A. N. Wright (2016), Solar prominences embedded in flux ropes: Morphological features and dynamics from 3-D MHD simulations, *Astrophys. J.*, *820*, 125, doi:10.3847/0004-637X/820/2/125.

Thompson, M. J., and A. N. Wright (1993), Resonant Alfvén wave excitation in two-dimensional systems—Singularities in partial differential equations, *J. Geophys. Res.*, *98*, 15,541–15,551, doi:10.1029/93JA00791.

Wright, A. N. (1992), Asymptotic and time-dependent solutions of magnetic pulsations in realistic magnetic field geometries, *J. Geophys. Res.*, *97*, 6439–6450, doi:10.1029/91JA02666.

Wright, A. N., and W. Allan (1996), Structure, phase motion, and heating within Alfvén resonances, *J. Geophys. Res.*, *101*, 17,399–17,408, doi:10.1029/96JA01141.

Wright, A. N., and T. Elsden (2016), The theoretical foundation of 3-D Alfvén resonances: Normal modes, *Astrophys. J.*, *833*, 230, doi:10.3847/1538-4357/833/2/230.

Wright, A. N., and I. R. Mann (2006), Global MHD eigenmodes of the outer magnetosphere, in *Magnetospheric ULF Waves: Synthesis and New Directions*, vol. 169, edited by K. Takahashi et al., pp. 51–72, AGU, Washington, D. C.

Wright, A. N., and M. J. Thompson (1994), Analytical treatment of Alfvén resonances and singularities in nonuniform magnetoplasmas, *Phys. Plasmas*, *1*, 691–705, doi:10.1063/1.870815.

Wright, A. N., W. Allan, R. D. Elphinstone, and L. L. Cogger (1999), Phase mixing and phase motion of Alfvén waves on tail-like and dipole-like magnetic field lines, *J. Geophys. Res.*, *104*, 10,159–10,176, doi:10.1029/1999JA900018.

Zalesak, S. T. (1979), Fully multidimensional flux-corrected transport algorithms for fluids, *J. Comput. Phys.*, *31*, 335–362, doi:10.1016/0021-9991(79)90051-2.